Patterns of precursory rockfall prior to slope failure

Nick Rosser,[1] Michael Lim,[2] David Petley,[1] Stuart Dunning,[1] and Robert Allison[3]

Received 24 July 2006; revised 23 July 2007; accepted 4 September 2007; published 19 December 2007.

[1] In this paper we examine data generated using high-resolution three-dimensional laser scanning monitoring of coastal rock cliffs. These data are used to identify spatial and temporal patterns in rockfall activity behavior prior to slope failure. Analysis of the data suggests that given sufficient measurement precision precursory behavior, here manifest as the rate of rockfall activity prior to failure, can be detected, measured, and monitored. Environmental conditions appear to have a diminishing influence on the occurrence of increasingly large slope failures. The monitoring data implies a time-dependent sequence in the occurrence of smaller rockfalls in the period leading to the largest failures recorded. This behavior is attributed to the mechanisms of strain accumulation in the rock mass resulting from brittle failure of the slope. The implication is that combining these data with models of failure mechanisms may allow failure time to be forecast from wide-area monitoring of precursory behavior. These findings have implications for the management of potentially unstable slopes, the understanding of slope failure mechanisms, and the generation of a new type of slope failure warning systems.

Citation: Rosser, N., M. Lim, D. Petley, S. Dunning, and R. Allison (2007), Patterns of precursory rockfall prior to slope failure, *J. Geophys. Res.*, *112*, F04014, doi:10.1029/2006JF000642.

1. Introduction

[2] Full risk assessment for slope hazards requires an understanding of likely geometry, triggers, failure dynamics and timing, but the last of these remains the most problematic to understand. The Leyte landslide in the Philippines on 17 February 2006 [*Evans et al.*, 2007] demonstrated that a good spatial awareness of slope hazard is commonly confounded by a poor awareness of the likely failure timing. Although the slope was known to be unstable and had previously been characterized as such, the relation between rainfall, precursory deformation and the ultimate timing of failure was poorly understood. The failure occurred five days after the period of highest intensity rainfall, a lag commonly observed in slope failures [*Adler et al.*, 2006]. High spatial and temporal resolution studies of rockfalls remain scarce [*Sass*, 2005a, 2005b; *Dussauge et al.*, 2003]. These studies tend to operate at one of two disparate scales; those concerned with general regional patterns of behavior [*Sass*, 2005a], and those intensive site-specific studies of individual failures [*Zvelebil and Moser*, 2001]. Both approaches aim to identify controls on rockfall occurrence in time and space. It is commonly neither practical nor effective to transfer the methods employed between these scales. It is also often difficult to compare statistically the event inventories from such studies. It is often the largest, indeed the most unusual events that have the highest impact, yet as it is these that normally have the least statistical representation in magnitude-frequency distributions, they remain the least predictable. An alternative line of enquiry to explain rockfall occurrence is the analysis of spatial and temporal patterns in precursory phenomena prior to large slope failure.

1.1. Precursory Behavior Prior to Rock Slope Failures

[3] Patterns in the precursory deformation of slopes, manifest in surface and subsurface displacement, have been widely observed and linked to the internal processes of brittle and ductile slope failure [*Main*, 2000; *Petley et al.*, 2005]. In a brittle first time failure, behavior is typically observed to adhere to the three phases of time-dependent creep: an initial accelerating period of strain termed transient creep (primary); a constant rate of strain termed steady state (secondary); and a final period resulting in failure by the localization of deformation termed accelerating creep (tertiary) [*Varnes*, 1983]. Notably, *Saito and Uezawa* [1961] observed from field monitoring that the final phase of failure in slopes is characterized by a hyperbolic function of velocity (v) against time (t), manifest by a straight line in v^{-1}-t space. This behavior has been suggested to mirror the nonlinear final stage of creep experienced in a brittle failure [*Petley*, 2004]. Understanding this behavior ultimately has the potential to allow the failure time to be estimated from whole-slope displacement monitoring [*Crosta and Agliardi*, 2003]. The time-dependent behavior of a slope undergoing brittle failure is similar to that observed in other natural systems including earthquake rupture propagation [*Main*, 2000], failures in deep mines and quarries [*Szwedzicki*, 2003], ice avalanches [*Pralong et al.*, 2005], and the evolution of some volcanic systems [*Kilburn*, 2005]. Several

[1] International Landslide Centre, Institute of Hazard and Risk Research, Geography Department, Durham University, Durham, UK.
[2] School of Civil Engineering and Geosciences, University of Newcastle upon Tyne, Newcastle, UK.
[3] University of Sussex, Sussex House, Brighton, UK.

0148-0227/07/2006JF000642

challenges remain in the wider application of this model, including: the cause of the transition of a failure from secondary to tertiary creep, the scale dependence of a critical level of strain development in a failure, and the challenge of appropriately monitoring the strain accumulation and its derivatives across a slope.

[4] *Voight* [1988] suggested that the power law acceleration in slope displacement should also be reflected in strain, seismicity and seismic energy release, suggesting that the surface expression of subsurface deformation processes is potentially diverse. The implication for monitoring of a complex natural rock mass is that point measurement instruments will invariably measure local-scale attributes of the wider slope failure, such as tension crack opening, toppling or slumping, rather than the general behavior of the slope. Furthermore, monitoring data may be subject to multiple superimposed influences, including seasonality [*Palus et al.*, 2004], and longer-term creep [*Crosta and Agliardi*, 2003], making difficult the identification of patterns in behavior that deviate from background levels.

[5] A limited number of studies have attempted to monitor precursory behavior at known unstable sites. *Amitrano et al.* [2005] established a network of seismic monitoring equipment in chalk cliffs at Menil-Val, Haute Normandie, France. A power law acceleration of seismicity rate and energy release across three orders of magnitude in the two hours prior to a failure of $1-2 \times 10^3$ m^3 was observed and similarities with observation of brittle failures in laboratory conditions were noted. Analysis of the distribution of microearthquake swarms using microseismic monitoring has been used to describe the geometry of a developing failure structure [*Fehler et al.*, 2001], and has been applied to large failing rock masses [*Willenberg et al.*, 2002]. *Zvelebil and Moser* [2001] used three case histories of large individual failures to suggest that time-dependent models such as that proposed by *Fuzukono* [1984] can be applied to predict successfully rockfall timing over short (days to weeks), medium (weeks to months) and long (months to years) periods. Semiquantitative accounts of accelerating behavior have also been widely documented at a range of scales. Increasing volumes of rockfall debris upon the surface of the Kolka Karmadon Glacier in September 2002 prior to its collapse were noted by *Huggel et al.* [2005], using satellite imagery. *Suwa et al.* [1991] and *Suwa* [1991] noted that the occurrence of precursory phenomena such as rockfall and small landslides increases with time prior to a large failure event in a Japanese quarry, suggesting that the level of precursory behavior is proportional to the ultimate failure magnitude. It is clear that precursory deformation via strain accumulation is reflected not just through creep and displacement, but also through increased shedding of slope surface material via rockfall in the period prior to failure. This evidence also suggests that precursory behavior may be scale-dependent and proportional to the ultimate failure magnitude, but this has not been quantified.

1.2. Environmental Controls on Rockfalls

[6] A common approach to explain rockfall is to analyze the environmental conditions that promote rockfall occurrence and those factors that initiate movement [*Dorren*, 2003]. These deterministic approaches are rarely able to predict the timing of individual events [*Dussauge-Peisser et al.*, 2002]. These approaches, led by *Rapp* [1960], have had success in linking for example temperature, specifically that relating the freeze thaw or the time the slope resides within the 'frost shattering window' [*Walder and Hallet*, 1986], seismicity [*Vidrih et al.*, 2001], weathering and bedrock type [*Day*, 1997], moisture availability [*Hall*, 1988], and morphological attributes such as aspect [*Sass*, 2005a], to the general patterns of rockfall occurrence. Most studies conclude that a combination of geotechnical, location and environmental factors lead to rockfall triggering [*Dorren*, 2003]. A second approach has been to develop probabilistic models based upon historic inventories [*Dussauge-Peisser et al.*, 2002]. These approaches have had considerable success in identifying consistent relationships in rockfall size and occurrence. Several problems remain. First, rockfall data is commonly collected from nets or traps at the slope toe. This assumes all material is transferred to the toe, the material size at the toe reflects that at the point of detachment and that the process of material detachment results in transfer to the slope toe, which as *Sass* [2005a] points out, in many situations, is two separate processes. Secondly, magnitude-frequency distributions generated from rockfall inventories are commonly subject to sampling deficiencies, with a cutoff at the smallest and largest size fractions as a result of the monitoring technique adopted. Relatively few studies deal with actual volume distributions of rockfall, possibly as a function of the semiqualitative nature of many rockfall inventories [*Dussauge et al.*, 2003; *Hungr et al.*, 1999] and the difficulties associated with precisely calculating volumes. What is perhaps surprising from studies that use these approaches is the diversity in rockfall triggers compared to the consistency in the character of the resulting rockfall inventories, as previously suggested by *Malamud et al.* [2004]. On slopes where material once failed detaches and is in free fall, rockfall magnitude-frequency distributions normally adhere to a linear relationship in log-log space, rockfalls invariably appear to occur without an apparent trigger, and there is a limited seasonal control on the detachment of rockfall blocks. Where a mismatch between the timing of a triggering event and a resulting failure is observed, the explanation is commonly surrendered to environmental complexity.

2. Field Site

[7] This study has been undertaken on the Jurassic cliffs of the coast of the North York Moors National Park, UK (Figure 1). The cliffs comprise near-horizontally bedded Jurassic limestones, shales and mudstones, capped by a sequence of Cretaceous sandstones and Quaternary glacial tills. The cliffs studied here approach vertical, ranging in height from 25 m to nearly 100 m. The large tidal range (6–7 m), monitored at Whitby 24 km to south by the British Oceanographic Data Centre, results in an extensive wave cut platform extending up to 500 m seaward at low tides. The cliffs have a predominantly northern aspect, so although sheltered from the prevailing southwesterly weather, they are exposed to easterly and northerly storm surges. Sea level reaches the toe of the cliff at 3 m above ordnance datum owing to the slope of the foreshore. Five-minute weather observations are collected by a UK Meteorological Office weather station at Loftus 3 km to the north of the

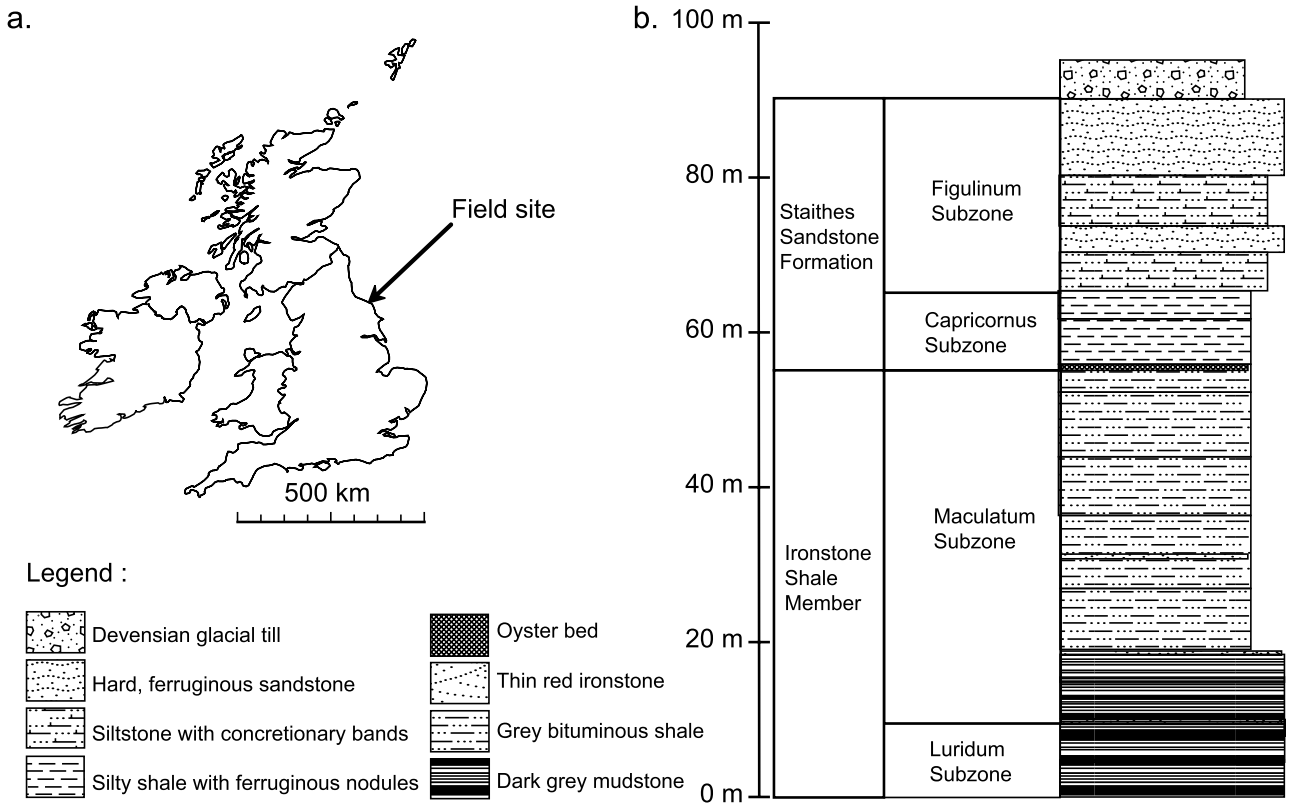

Figure 1. (left) Field site location at Staithes on the northeastern UK coast. (right) Geological section of the cliff exposure, showing height above ordnance datum [after *Howarth*, 1992].

village of Staithes, and are analyzed here for the period from 1991 to 2005. Average annual rainfall is 567 mm, with peak hourly intensities reaching 79.1 mm hr^{-1} in February. Minimum temperatures are moderated by the marine climate, but reach their mean daily minimum in January (−6°C), with spells of up to 11 days with mean air temperatures remaining below freezing. The largest diurnal temperature differential of 22°C normally occurs during May. Peak wind speeds can reach 135 km hr^{-1}, and when from the north waves at the 18 m bathymetric contour (approximately 1500 m offshore) have been observed by a wave buoy in excess of 10 m with a 50-year return period.

[8] The cliffs appear to be actively eroding, through a process of cliff toe abrasion through wave action and rockfalls of a wide range of sizes from across the face of the cliff. Rates of cliff face retreat have previously been calculated using a 110-year archive of maps and aerial photography, discussed by *Lim et al.* [2005]. This approach yields a rate of retreat of the cliff top of 0.1 m a^{-1} [*Agar*, 1960]. More recently surveys have been conducted using detailed terrestrial photogrammetry and LiDAR, yielding average cliff retreat rates of between 0.001 and 0.01 m a^{-1} [*Lim et al.*, 2005].

3. Methodology

[9] Six cliff sections totaling in excess of 100,000 m^2 of exposed rock face were resurveyed at monthly intervals for a period of 32 months, beginning in September 2002. Terrestrial laser scanners (MDL LaserAce600 and Reigl LMS420z) are used to collect a high-resolution point cloud across the cliff with average point spacing of 0.05 m, from the foreshore platform. The methodology of data collection employed is described by *Rosser et al.* [2005] and *Lim et al.* [2005]. Successive point clouds are georeferenced and positioned using an iterative closest points alignment algorithm, which achieves a RMS separation between scans of <0.02 m; the error here is associated with differences in scanned point positions on the cliff between scans rather than with errors in resetting the survey. Surface models are generated using a view-dependent triangulation algorithm, constructed from the look direction of the scanner. Mesh-to-mesh or Hausdorff distance is calculated and then projected onto a vertical plane parallel to the dominant plane of the cliff face. The values are rasterized to a 0.1-m grid, thus creating a difference image from which volumes of rockfalls are extracted using threshold filtering and an object oriented classification based upon the measurement precision obtainable from the laser scanner. Using this method, change in any given grid cell in the difference image identified between each monitoring visit is considered a single event, rather than two or more superimposed upon each other. This process is performed within Archaeoptics Ltd Demon3D and Research Systems Inc. ENVI RunTime 4.2. Further attributes of individual failures including geometrical derivatives and geological characteristics are calculated by analysis of the difference image using GIS, where the cliff height and width are projected in x and y coordinates, respectively. This size of objects detectable using this approach is a function of the angular and distance precision

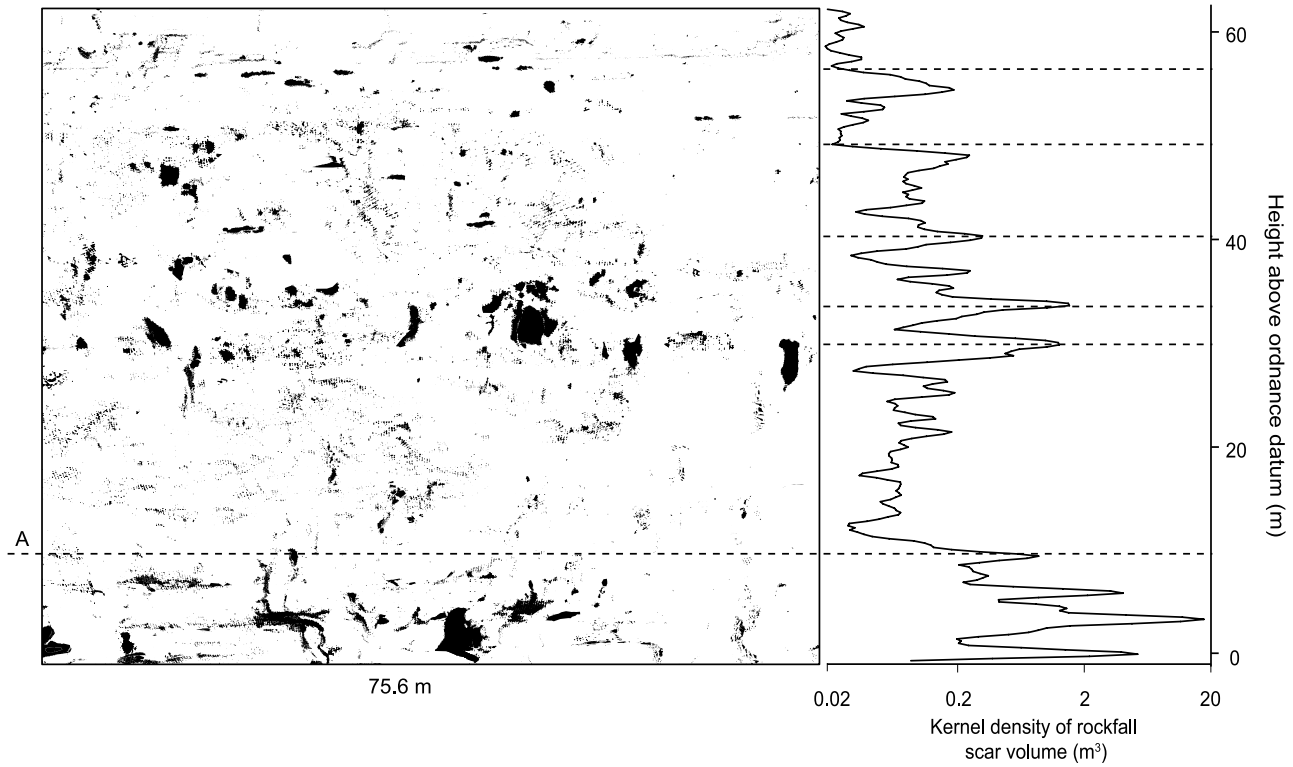

Figure 2. Example of output of laser scanning data, showing changes at site 1 for the entire monitoring period. The rock face is approximately 75 m wide and 70 m high, displayed as a view looking onto the cliff face. (left) Black areas indicate rockfall scars, with line A representing the highest level of wave inundation at this site (right) Kernel density estimate (Epanechnikov kernel, half width = 0.25 m) of rockfall activity up the cliff profile for all sites, with major lithological boundaries marked by dashed horizontal lines.

of the laser and survey resolution, as discussed by *Abellan et al.* [2007]. The analysis of the characteristics of the laser allows a confidence threshold to be placed upon the measurement of changes normal to and across the rock face [*Lim et al.*, 2005]. Tests demonstrate that using this approach at this scale of investigation, typical changes to the rock face of >0.00001 m^3 can be measured in three dimensions.

4. Results

4.1. General Observations

[10] The general pattern of rockfall from the cliffs shows scars distributed from all parts of the cliff face, an example of which is given in Figure 2. Once detached, material falls to the cliff toe with effectively zero storage of detached material on the cliff face owing to the near vertical slope. It is notable that all of the cliff face is potentially subject to change throughout the monitoring period. Only moderately increased levels of material detachment are measured at the cliff toe in the zone of wave impact that extends up to 6.5 m from the toe under still water conditions. Change is concentrated within the exposure of bands of specific lithologies and at structural discontinuities, in particular at boundaries between rock layers. Change appears to occur along feature edges on the cliff face, such as overhangs, protrusions or the outside perimeters of existing concavities. As such, the occurrence of rockfalls appears in general to accentuate preexisting features. Relative retreat of the rock face across all sites for the dominant rock types return variable aggregate rates during the monitoring period (sandstone (0.6 mm a^{-1}); siltstone (2.0 mm a^{-1}); shale (2.5 mm a^{-1}); mudstone (2.2 mm a^{-1})); rates that appear to conform to material competence and structure. There is no historic map evidence of a long-term change in the cliff profile form so ultimately these rates must converge over time to enable parallel retreat. The data show an apparently low connectivity between the activity at the cliff toe and the remainder of the cliff, with only limited evidence of the propagation of failures from the toe upward through time. This questions the role of wave notch development in dictating the nature of change to these cliffs. The geometry of individual rockfall appears to be influenced by the preexisting rock mass structure, with failure commonly detaching blocks defined by joints, where failures rarely straddle more than one rock type. The distribution of detachments varies little across the cliff face. Through time there appears to be only a limited seasonal control upon the occurrence of rockfalls, with events >1 m^3 occurring in all months of the year (Table 1). No significant seasonal pattern in total volumes or size and shape characters of rockfalls is detectable. Total volumes lost in each calendar month vary considerably between successive years.

Table 1. Rockfall Geometry, Volume, and Area Statistics, Categorized by Rock Type and Month of the Year

	Variable	All	Mudstone	Shale	Siltstone	Sandstone	January	February	March	April	May	June	July	August	September	October	November	December
Volume, m^3	mean	0.061	0.226	0.018	0.239	0.005	0.348	0.087	0.121	0.038	0.006	0.006	0.006	0.019	0.010	0.040	0.043	0.005
	min	0.000	0.000	0.000	0.000	0.000	0.000	0.000	0.000	0.000	0.000	0.000	0.000	0.000	0.000	0.000	0.000	0.000
	max	2614.880	1776.600	355.548	2614.880	6.515	2614.880	1776.600	1215.200	328.895	1.802	2.660	40.571	18.937	25.886	329.413	355.548	4.716
	sd	9.289	16.126	1.862	24.685	0.446	29.916	11.230	11.105	2.513	0.063	0.067	0.355	0.362	0.287	2.972	3.212	0.071
Area, m^2	mean	0.028	0.066	0.169	0.062	0.013	0.089	0.027	0.043	0.018	0.015	0.014	0.005	0.029	0.012	0.041	0.041	0.012
	min	0.000	0.000	0.000	0.000	0.000	0.000	0.000	0.000	0.000	0.000	0.000	0.000	0.000	0.000	0.000	0.000	0.000
	max	569.840	350.210	248.500	569.840	12.990	569.840	350.210	293.310	37.810	3.240	3.980	35.910	15.990	13.930	226.430	248.500	8.520
	sd	2.211	3.477	1.260	5.383	0.189	6.522	2.242	2.727	0.392	0.134	0.124	0.297	0.398	0.173	2.115	2.266	0.135
Cross cliff scar length, m	mean	0.086	0.109	0.072	0.078	0.091	0.097	0.085	0.103	0.099	0.087	0.097	0.026	0.118	0.088	0.099	0.092	0.085
	min	0.010	0.009	0.010	0.010	0.010	0.010	0.010	0.010	0.010	0.010	0.010	0.010	0.010	0.010	0.010	0.010	0.010
	max	66.890	66.890	25.920	25.740	9.690	25.740	66.890	56.370	17.470	5.100	6.540	14.720	9.690	4.600	21.920	25.920	8.370
	sd	0.346	0.759	0.205	0.292	0.209	0.349	0.479	0.576	0.284	0.203	0.205	0.153	0.276	0.160	0.302	0.330	0.181
Up cliff scar height, m	mean	0.073	0.078	0.065	0.070	0.076	0.086	0.071	0.079	0.081	0.079	0.086	0.023	0.098	0.081	0.086	0.079	0.075
	min	0.003	0.009	0.010	0.010	0.010	0.010	0.010	0.010	0.003	0.010	0.010	0.010	0.010	0.010	0.010	0.010	0.010
	max	34.430	15.110	21.470	34.430	3.580	34.430	15.110	14.210	8.850	3.560	2.660	7.150	4.500	5.500	21.470	13.760	4.000
	sd	0.209	0.296	0.162	0.348	0.123	0.423	0.171	0.213	0.190	0.167	0.140	0.091	0.212	0.130	0.281	0.248	0.135
Depth of scar, m	mean	0.565	0.050	0.074	0.031	0.035	0.065	0.074	0.035	0.033	0.042	0.025	0.063	0.068	0.069	0.064	0.057	0.054
	min	0.000	0.000	0.000	0.000	0.000	−0.370	−1.380	−1.950	−1.740	−1.160	−0.480	−1.290	−1.130	−0.490	−0.780	−1.100	−0.710
	max	18.790	18.790	8.180	10.680	3.830	10.680	18.790	5.110	4.910	4.790	4.730	8.340	4.540	8.110	6.630	9.150	9.150
	sd	0.701	0.872	0.738	0.416	0.371	0.756	0.726	0.594	0.538	0.609	0.539	0.717	0.783	0.842	0.688	0.684	0.675
Total	number	513576	115555	327148	54952	17461	68245	46512	17758	71881	31374	30040	47075	37338	78038	24940	30058	30317

4.2. Rockfall Area, Volume, Magnitude, and Frequency

[11] The mean rockfall volume is 0.061 m^3, with a median value of 0.0004 m^3, a standard deviation of 9.289 m^3, and the largest event measured 2614.88 m^3. Mean rockfall size and standard deviation varies considerably between rock types, with shales and sandstones detaching blocks an order of magnitude larger than those sourced from siltstones and mudstones (Table 1). Although there is an increase in mean volume during January and February compared to the rest of the year, there is no clear seasonality in rockfall volume or area. This is also reflected in rockfall geometry, as expressed by scar height and length across the cliff face, and the depth of the scar measured normal to the cliff face. Scar height varies more than both scar length and depth, both of which are remarkably consistent through the year, as described by the standard deviation. Rock type holds some control over rockfall geometry, particularly the depth of the failure into the rock face, whereby failures in the shales are approximately twice as deep as those failures in the siltstones and sandstones. Failures are in general wider and higher than they are deep, with ratio of mean scar length to height of 1.40, and ratio of mean scar length to depth of 2.18, suggesting that the majority of rockfalls represent the removal of surface material, rather than deeper seated failure.

[12] The relationship between the measured rockfall volume and the area of the rockfall scar (measured across a plane parallel to the rock face) equates to a power law relationship of the form $V = kA^{\alpha}$, where $\alpha = 0.982$ and $k = 0.232$. This obtains a significant r^2 value of 0.51 for the total 513,576 rockfalls. This is similar in form to area volume relationships made for other landslide inventories, for example, *Simonett* [1967] and *Hovius et al.* [1997]. This approach does assume that within the 1 month sampling window rockfalls are not superimposed; an effect that may ultimately underrepresent the relative contribution of small events. The cumulative frequency distribution (Figure 3) of all rockfalls in the inventory shows a smooth curve, suggesting that the changes observed form a continuum of events across all size fractions. The cumulative distribution for all events adheres to a linear trend in log volume versus normalized frequency space, of the form $frequency = kLn(volume) + b$, where $k = 0.1548$, $b = 1.726$, which obtains a significant r^2 value of 0.998 over 2 orders of magnitude between 0.0005 m^3 and 0.05.m^3. Beyond this range the scale-invariant behavior breaks down for both small and large events. Cumulative frequency curves for the different rock types in the cliff profiles also indicate some variability in behavior, with a range of scaling exponents (b) across the 0.0005 m^3 to 0.05 m^3 size range (shale $b = 1.910$ ($r^2 = 0.996$); sandstone $b = 1.737$ ($r^2 = 0.976$); mudstone $b = 1.430$ ($r^2 = 0.995$), and siltstone $b = 1.692$ ($r^2 = 0.989$)). All b values obtained here are higher than those established elsewhere for rockfall only inventories [*Hergarten*, 2003]. The exponent value for this same size fraction for each month of the year has an equally high standard deviation (0.379). Although there is no consistent seasonal variation in the exponent value, the two lowest values (1.120 and

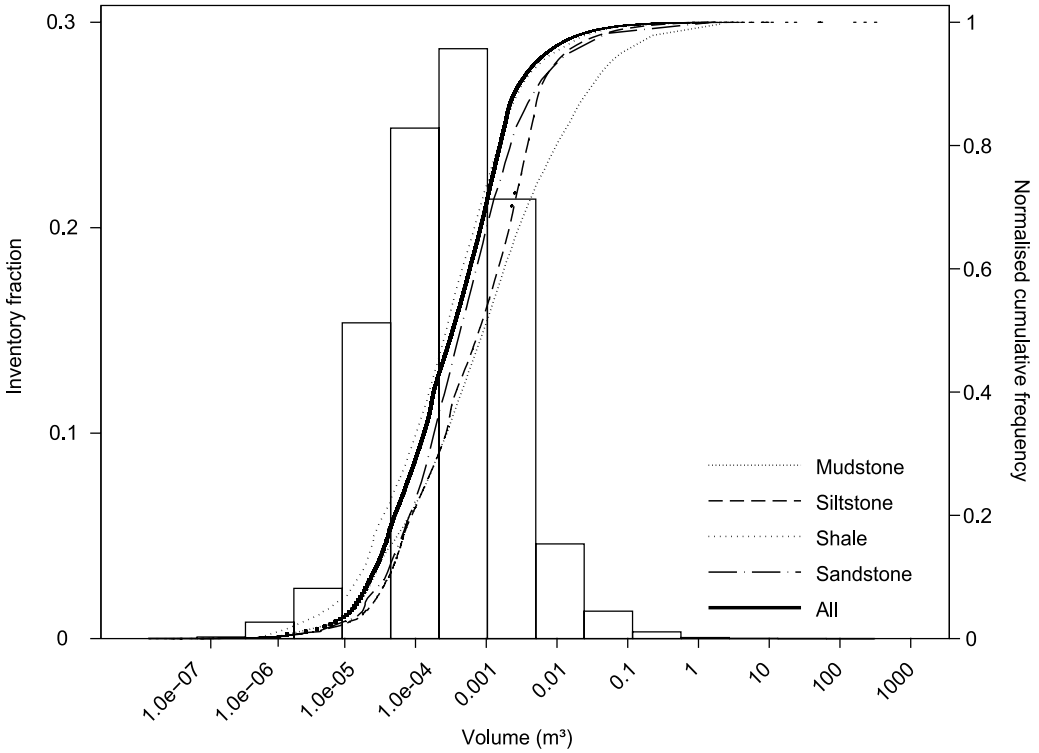

Figure 3. Normalized cumulative magnitude frequency distributions for rockfall volumes, showing curves for all rockfalls, and the inventory categorized by rock type. Histogram illustrates the relative contribution of size fractions to the overall inventory, with bins uniformly distributed in log(volume) coordinates, and rockfall frequency within bins normalized to bin width.

1.531) occur in July and June respectively and the two highest values (2.366 and 2.316) occur in December and February. The histogram in Figure 3, whereby the histogram bins are in logarithmic coordinates with the numbers of events normalized by bin width, indicates the relative contribution of the size fractions in the rockfall inventory.

4.3. Environmental Controls on Rockfall and Their Scale Dependence

[13] Environmental data describing local onshore wind, temperature, rainfall, insolation and tidal conditions is at 15-min intervals. Onshore weather data is obtained from a UK Meterological Office weather station, 2 km from the monitoring sites, and tidal data collected at a UK Hydrographic Office gauges at Whitby and Teesside, each approximately 20 km from the monitoring site. For each month, mean, peak and cumulative environmental variables are calculated, as described in Table 2. Variables are derived that have been shown elsewhere to hold a significant influence over rockfall triggering. A least squares regression analysis is then undertaken to correlate these environmental variables to both the occurrence and characteristics of rockfalls. For this analysis the rockfall inventory is categorized first by time, testing the direct correlation between any given month (M) and the environmental conditions during that month, secondly by using direct lag times where ($M - n$) is considered (where n is 1, 2, 3, 4, 5, and 6 months), and thirdly by analyzing cumulative lag effects, where rockfalls in months M to ($M - n$) inclusive are considered (where n is 1, 2, 3, 4, 5 and 6 months). A maximum time span of 6 months is employed to maintain the significance of relationships derived at the beginning of the monitoring period, hence where ($M - n$) or (M to ($M-n$)) is negative the number of samples is less. The data are further categorized based upon the four dominant rock types (mudstone, sandstone, siltstone and shale), by discrete size fraction (>1 m^3, 1 m^3–0.1 m^3, 0.1 m^3–0.01 m^3, 0.01 m^3–0.001 m^3, 0.001 m^3–0.0001 m^3, 0.0001 m^3–0.00001m^3 and <0.00001 m^3), and by monitoring site (1 to 6). The results of the least squares regression analysis are presented in Table 2.

[14] Insignificant relationships are obtained between environmental variables and rockfall, both through direct correlations between rockfall occurrence and prevailing weather conditions and those with lagged or cumulative effects. Out of a total of 493 regression tests shown in Table 2, only six return significant results. Mean and peak wind velocity derived three of these significant relationships, but these are confined to specific sites and are not transferable beyond. A significant relationship is also found between failures from the mudstone and the level of the mean monthly high tide. Interestingly it is the mudstones that commonly form the foot of the cliff exposed to marine action. The remaining significant correlations are found between the shale rocks that form the majority of the cliff face, and the minimum monthly temperature, and secondly there is a significant inverse relationship between the mean monthly temperature and rockfall occurrence at site 3. No significant relationships are found between specific rockfall size fractions and the environmental drivers, and no significant variation in the response of different rock types to environmental forcing is discernable. The degree of variability in rockfall activity does not reflect that of the environmental characteristics that have been shown in other situations to drive rockfall detachment, an observation also noted by *Sass* [2005b].

[15] Further categorizing the rockfall inventory assesses the scale dependence of rockfall occurrence in response to prevailing environmental conditions. Analysis of the correlations for size fractions <0.0001 m^3, and 0.0001–0.001 m^3 and 0.001–0.01 m^3 respectively, with mean and peak monthly wind velocity, minimum monthly temperature, hours below freezing, mean and peak monthly rainfall, mean monthly insolation, and all tidal variables is undertaken. Although statistically insignificant, all correlations reduce in significance as increasingly large rockfalls are analyzed. This trend is analyzed further by categorizing the inventory by volume, whereby all rockfalls below threshold levels are included within the correlation. Figure 4 shows this analysis for 11 variables. The nature of change in correlation strength, although in most tests statistically insignificant, suggests in many cases a volume threshold between 0.001 and 0.01 after which the intensity of the environmental driver holds little control over the resultant occurrence of rockfall. Although the number of large rockfalls in the data set is relatively small, their number still remains significant, yet deterministic approaches do not appear appropriate for modeling their timing.

4.4. Precursory Behavior

[16] In the absence of strong correlations between large rockfalls and the environmental variables, the temporal patterns of rockfalls across the rock face in the months prior to the largest slope failures recorded are assessed. This is undertaken in an attempt to quantify previous observations of increasing rockfall activity prior to large rock slope failures. The 10 largest discrete failures from the rockfall inventory are identified and from the period from the start of the monitoring to the occurrence of the rockfall, a sampling window is delimited with the same coverage on the cliff face as the final failure. Rockfalls with centroid located within this sample window in the months prior to failure are analyzed, as shown in the example in Figure 5. Only those rockfalls with scar areas that fall entirely within the monitored cliff face are included to reduce edge effects in the analysis. A scale-free measure of rockfall behavior in the months prior to ultimate failure is derived using the monthly volume of detachments per square meter within this zone. As such, it assumes that precursors may occur over an area wider than the final failure owing to sampling based upon the precursor centroid rather than its ultimate extent.

[17] This analysis shows an increase in rockfall activity for the majority of the 10 largest rockfalls recorded in the monitoring. An example of the sequence of precursors is given in Figure 5, showing the concentration of detachments in the zone of the ultimate failure and the absence of change in surrounding areas. The 8 months preceding failure (Figures 5a–5h) are shown, with the next 3 month period following (Figures 5j–5l). In many instances it is also apparent that the precursors themselves occur within zones that have previously experienced smaller failures (e.g., those rockfalls shown in Figures 5f–5h). It is also clear that in the months preceding the failure, smaller

Table 2. Correlation Statistics Describing the Links Between Rockfall Occurrence and Environmental Conditions

Environmental Correlations	Correlation	Number of Samples	Mean Wind Velocity, m s^{-1}	Peak Monthly Wind Velocity, m s^{-1}	Total Wind Run, m	Mean Monthly Temperature, deg	Minimum Monthly Temperature, deg	Hours Below Freezing	Mean Monthly Rainfall, mm	Monthly Rainfall Total, mm	Peak Monthly Rainfall Intensity, mm hr^{-1}	Mean Monthly Insolation, W m^{-2}	Peak Monthly Insolation, W m^{-2}	Monthly Sum of Isolation, W m^{-2}	Maximum Monthly High Tide, m	Monthly Peak Tidal Range, m	Monthly Mean Tidal Range, m	Hours Tide 3 m, hours
Total	Volume (m^3)	513576	−0.004	−0.006	0.001	0.006	0.003	0.002	0.010	−0.005	0.003	0.006	0.004	0.005	0.003	0.002	0.002	0.001
Lagged conditions	Volume−(M−1)	487912	0.003	0.005	−0.001	−0.004	−0.004	0.000	0.020	0.002	0.001	0.003	0.004	0.003	−0.005	−0.001	0.004	−0.001
	Volume−(M−2)	468721	0.013	−0.001	−0.001	−0.004	−0.006	0.005	0.005	−0.001	−0.001	0.004	0.004	0.003	−0.002	−0.001	0.007	−0.001
	Volume−(M−3)	410789	0.004	0.000	−0.001	−0.001	0.000	0.001	0.002	0.002	−0.001	0.002	0.004	0.003	0.001	−0.001	0.006	−0.001
	Volume−(M−4)	386152	0.003	−0.002	−0.001	0.004	0.004	−0.004	0.001	−0.002	0.006	−0.001	0.004	0.003	0.003	−0.001	0.005	−0.001
	Volume−(M−5)	377215	−0.002	−0.001	−0.001	0.009	0.008	−0.005	0.001	0.002	0.004	−0.004	0.004	0.003	0.002	−0.001	0.003	−0.001
	Volume−(M−6)	345410	−0.007	−0.007	−0.001	0.008	0.009	−0.004	0.010	0.001	0.006	−0.004	0.004	0.003	−0.003	−0.001	0.000	−0.001
Cumulative conditions	Volume−(M to M−1)	487912	−0.117	0.150	0.000	0.026	0.174	−0.185	0.007	−0.584	−0.172	0.058	0.006	0.005	0.164	0.002	0.227	0.010
	Volume−(M to M−2)	468721	−0.123	0.077	0.009	0.127	0.186	−0.223	0.005	−0.614	0.126	0.012	0.003	0.007	0.277	0.001	0.211	0.020
	Volume−(M to M−3)	410789	−0.183	0.080	0.002	0.210	0.261	−0.288	0.004	−0.593	0.146	0.001	0.000	0.000	0.264	0.001	0.174	0.018
	Volume−(M to M−4)	386152	−0.217	−0.010	0.008	0.223	0.279	−0.247	0.002	−0.448	0.168	0.023	0.002	0.000	0.136	0.008	0.136	0.007
	Volume−(M to M−5)	377215	−0.144	−0.090	0.006	0.246	0.271	−0.262	0.002	−0.340	0.064	0.015	0.007	0.000	0.099	0.004	0.101	0.004
	Volume−(M to M−6)	345410	−0.178	−0.133	0.005	0.237	0.268	−0.316	0.001	−0.140	0.166	0.015	0.004	0.000	0.004	0.005	−0.010	0.002
Rock type	Mudstone	115555	0.017	0.256	0.008	−0.594	−0.535	0.325	0.002	−0.215	−0.671	0.004	0.006	0.008	0.735	0.009	−0.422	0.006
	Sandstone	17461	0.644	−0.197	0.007	−0.217	−0.233	0.253	0.006	−0.097	0.066	0.001	0.008	0.009	0.237	0.002	0.339	0.005
	Siltstone	54952	0.126	0.344	0.008	−0.143	−0.117	−0.014	0.004	−0.078	−0.099	0.001	0.009	0.009	−0.140	0.007	−0.132	0.005
	Shale	327148	−0.221	−0.242	0.006	0.713	0.750	−0.451	0.008	0.475	0.340	0.007	0.004	0.002	−0.055	0.004	0.290	0.002
Rockfall size, m^3	> 1	36	0.008	0.143	0.007	−0.121	−0.080	0.032	0.000	0.000	−0.170	0.001	0.003	0.000	0.154	0.000	0.044	0.002
	0.1−1	184	0.053	0.098	0.000	−0.075	−0.065	0.058	−0.197	−0.197	0.058	0.004	0.002	−0.197	0.122	−0.197	0.053	0.001
	0.01−0.1	15552	0.064	0.105	0.009	0.005	0.003	0.013	0.062	0.062	−0.059	0.005	0.000	0.062	−0.011	0.062	0.104	0.009
	0.001−0.01	142554	0.050	−0.028	0.007	0.004	0.012	0.063	0.002	0.002	0.053	0.004	0.002	0.002	−0.160	0.002	0.115	0.004
	0.0001−0.001	166374	0.123	−0.133	0.008	0.088	0.056	−0.058	0.095	0.095	−0.028	0.008	0.009	0.095	−0.046	0.095	0.096	0.006
	<0.0001	188881	0.123	−0.133	0.009	0.088	0.056	−0.058	0.095	0.095	−0.028	0.009	0.000	0.095	−0.046	0.095	0.096	0.011
Site	1	87236	0.026	−0.082	0.002	−0.032	0.016	−0.086	−0.108	−0.108	−0.152	0.006	0.008	−0.108	0.529	−0.108	−0.183	0.006
	2	13247	0.815	−0.402	0.004	−0.264	−0.275	0.280	−0.372	−0.372	0.019	0.002	0.009	−0.372	0.263	−0.372	0.080	0.005
	3	4088	0.272	0.656	0.003	−0.722	−0.659	0.438	−0.222	−0.222	−0.668	0.009	0.007	−0.222	0.374	−0.222	−0.466	0.009
	4	222450	0.285	0.352	0.001	−0.442	−0.364	0.563	0.242	0.242	−0.326	0.009	0.005	0.242	0.376	0.242	0.219	0.001
	5	72798	0.955	−0.745	0.003	−0.125	−0.326	0.219	−0.286	−0.286	0.294	0.008	0.003	−0.286	0.007	−0.286	0.364	0.007
	6	113755	−0.095	0.103	0.009	0.053	0.190	−0.133	0.282	0.282	−0.137	0.006	0.001	0.282	0.181	0.282	0.189	0.005

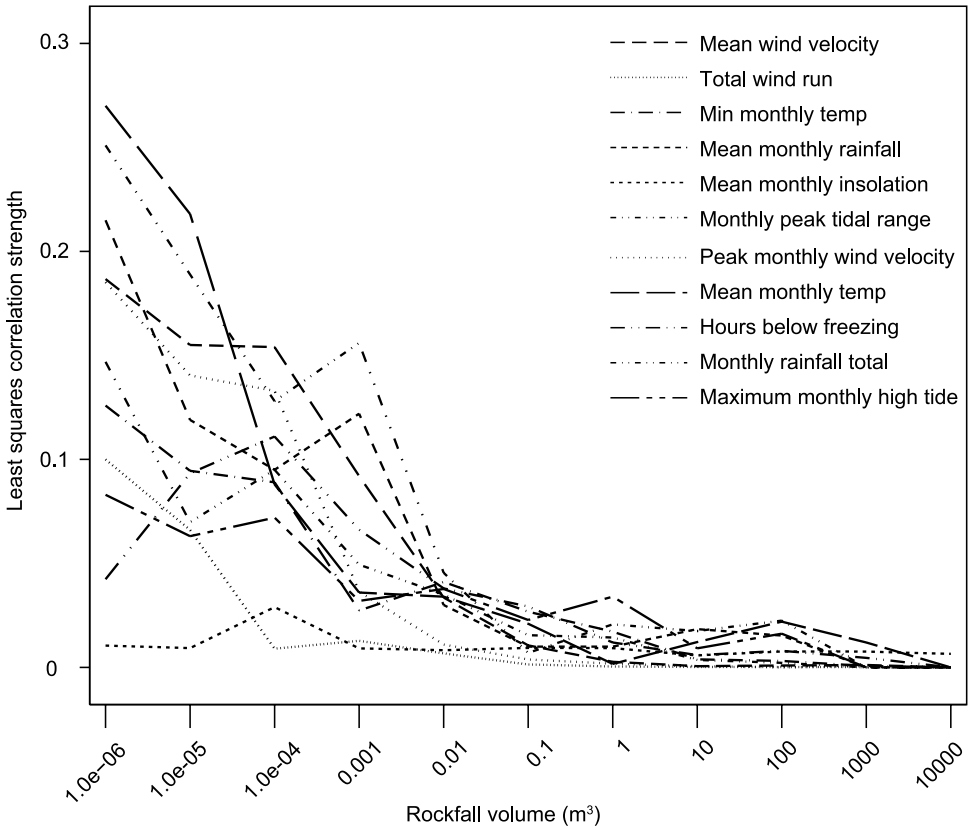

Figure 4. Graph illustrating the decrease of the least squares correlation r value between environmental variables and increasingly large rockfalls, for a range of monitored environmental variables.

rockfalls are concentrated in the areas around the edges, particularly the lower extent, of the final failure scar. Several of the largest rockfalls display a three-phase type pattern, with an initial loss of material, followed by a secondary period of relative quiescence or lower rate of activity, that finally accelerates into a tertiary period of increased rockfall activity in the months immediately prior to final failure. The months after failure have relatively low levels of activity (Figures 5j–5l). It is also apparent at this sampling interval that there is greater linearity in the increased behavior prior to larger events. In general both of these patterns are more pronounced prior to the largest rockfalls described in Figure 6 (>100 m^3). This suggests that the time prior to each failure during which there is an increase in rockfall detachment away from a base level increases with final failure volume. For rockfalls <100 m^3 precursory behavior, defined as a clear departure from a background level, is apparent only within the one or two month period prior to failure. The volume of material detached in the months preceding the ultimate failure is also proportional to the volume of the final failure. Figure 7 illustrates this observation for the largest 1000 rockfalls (volumes > 0.157 m^3), showing a direct linear relationship between the rockfall volume in M and that in the same area during (M-1). Hence the larger failures appear to be preceded by a greater number of rockfalls of a larger volume than those preceding the smaller failures (Figures 5 and 7). Precursory rockfall are therefore scale-dependent phenomena both through time and across space.

5. Discussion

[18] The data presented have implications for the understanding of how these coastal cliffs change and evolve. Despite recording over 500,000 rockfalls only a small number of these events (<100) resulted in any change to the planform of the cliff line, and the majority of these events resulted in changes smaller than those identifiable from sequences of aerial imagery and maps. The treatment of such planform data for assessment the magnitude and frequency of retreat and change on subvertical rock faces therefore masks considerable and significant levels of activity. The data suggest that there is a limited difference in the behavior of the section of the cliff inundated by the sea during high tides, relative to that permanently exposed above. In this instance the role of classical wave cut notch development in dictating the rate and nature of coastal cliff retreat is questionable. A clear rock control in rockfall shape and size has been shown, with varying mean rates of retreat calculated for the four rock types examined at these sites. In the absence of a long-term alteration of the cliff profile form, these rates must ultimately tend to converge. The behavior observed between sites, despite variations in cliff height, relative elevation, morphology and setting, is consistent in terms of both aggregate frequency distributions and total rates of change in addition to consistent rockfall

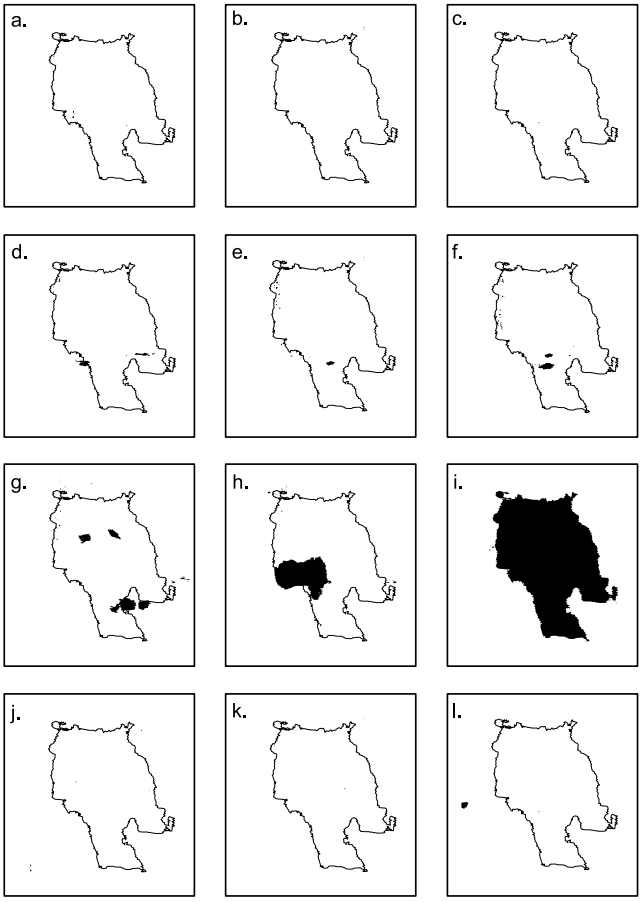

Figure 5. Sequence of rockfalls recorded in the months November 2004 to June 2005, prior to a large failure (25.9 m^3) in July 2005. Each image, covering 1 month, shows a view looking normal to the dominant plane of the cliff face, depicting changes monitored within an area 10 m × 11.5 m. Black areas show rockfall scars, with the extent of the large rockfall in Figure 5i superimposed over each month.

geometry and source rock. This suggests that the frequency of the largest events can be estimated by analysis of the smaller events, and that the nature of the distribution is likely to remain consistent during a longer monitoring period. This is of value when considering both historic changes to the coast, but also to a consideration of future conditions, as previously suggested by *Guzzetti et al.* [2003] for rockfalls in the Yosemite Valley, California.

[19] The magnitude and frequency of rockfalls derived from the monitoring suggests that changes to coastal rock cliffs adhere to characteristic scale-invariant behavior observed in other rockfall inventories [*Malamud et al.*, 2004; *Guzzetti et al.*, 2002], albeit across a limited range of event magnitudes. This limited range is not however unusual in other theoretical instances, for example *Densmore et al.* [1998]. In light of the apparent acceleration in rockfall activity prior to a large slope failure, it is sensible to assume that the smaller size fraction is underrepresented in this inventory owing to the relatively coarse temporal window interval and rockfall superimposition. *Amitrano et al.* [2005] noted a 3 orders of magnitude increase in seismic energy release in the 2 hours leading to failure. At the survey

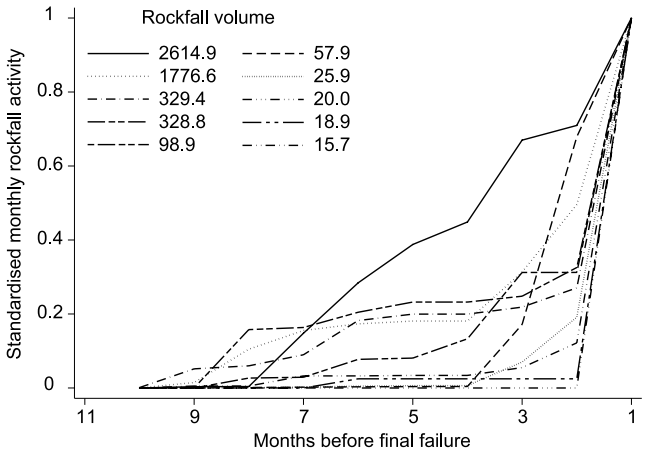

Figure 6. Graph illustrating the increase in rockfall activity prior to the 10 largest failures recorded. Volumes of the final failures are given in the legend in m^3. (Rockfall activity is here displayed as the mean volume of material lost per month per meter square of the rock face within the area of the "sampling" window. This measure is standardized to the rate measured in the month prior to failure to allow scale-free comparison of the behavior between rockfall of different sizes.)

interval employed here, much of this activity, which results primarily in small size rockfalls, would not be captured. It may therefore be reasonable to expect the scale-invariant behavior observed to extend over a wider range of event magnitudes in a complete inventory.

[20] Considerable debate surrounds the underlying reasons for the power law behavior observed in rockfall and landslide inventories. *Dussauge et al.* [2003] explore this by comparing erosion-type models [*Densmore et al.*, 1998] with fragmentation models [*Turcotte*, 1997] and conceptual sandpile-type models [*Bak et al.*, 1987]. *Hergarten* [2003] argues the use of these models, notably those reliant upon self-organized criticality, remains difficult in terms of maintaining their physical consistency

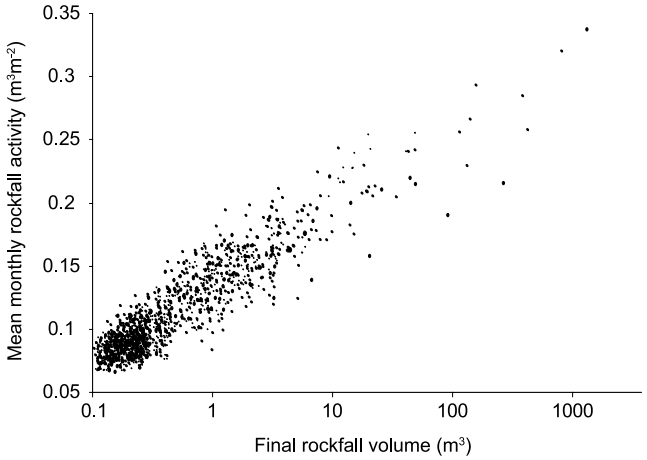

Figure 7. Graph showing the relationship between the final rockfall volume and the mean monthly rate of rockfall activity monitored in the month prior to failure for the largest 1000 rockfalls in the inventory (> 0.157 m^3).

and quantitative success, often resulting in an over-significance of the largest events. *Hergarten* [2003] suggests that such models are considerably improved by the introduction of time-dependent material properties, notably weakening, such as that experienced during the coalescence and localization of deformation during progressive failure [*Bjerrum*, 1967]. In such a model it is sensible to assume that the magnitude-frequency distribution of events will vary, particularly during a brief sampling period. During a sampling period that is short compared to the return period of all possible events in any given environment, an inventory may only capture part of a sequence of events due to weakening, and hence only a limited range of magnitudes. In many inventories this effect maybe counteracted by contiguous sections of rock face being concurrently weakened to different degrees. Hence an inventory from even a relatively small rock face may capture a full magnitude-frequency distribution as a product of rockfalls sourced from different sections of rock face at different stages of progressive failure. In part this supports the model of *Densmore et al.* [1998] that assumes a failure size control that is dependent on the time period since the last failure of any given slope. The logical corollary to such inventory power law behavior is temporal sequences of events that reflect this weakening, manifest via precursors.

[21] In mixed-type landslide inventories the coalescence of metastable slopes has been suggested as a reason for this power law relationship at the landscape scale [*Turcotte*, 1997; *Malamud et al.*, 2004]. This may also be applicable to a rockfalls from a failing and fragmented rock mass, wherein detachments appear to accentuate existing unstable morphological features such as protrusions or overhangs. Over time, features coalesce via fracturing of the rock mass to form larger formations, shedding precursors, until the subsequent larger-scale failure. This accelerating behavior representing a power distributed release of energy has also been observed in the localization of deformation onto a plane during brittle failure, attributed to microcrack coalescence and build up of damage [*Main*, 2000], and is applied widely in seismicity and may have application to mass movements [*Hergarten*, 2003; *Grasso and Sornette*, 1998]. If this process in rock masses results in strain accumulation, similarly increasing levels of disruption and hence numbers rockfalls are likely. The magnitude-frequency distribution may therefore be both a product of the fragmentation and disintegration of the rock mass as defined by structurally delimited preexistent fragments. This is possibly accentuated by a feedback between the rockfalls perpetuating the conditions that lead to further larger rockfalls on the rock mass surface. In this instance the difference in the magnitude-frequency power exponent between different rock types maybe substantiated by the relative importance of these two factors within the various rock bands monitored.

[22] Thresholds above which environmental conditions have no discernable influence have been identified and the apparent insensitivity of large failures to environmental drivers has been quantified. The rockfall inventory may therefore be a composite of two populations of events that are scale-dependent in their response to environmental drivers. Environmental variables, shown in previous studies to have a significant control upon rockfall occurrence, have been tested and shown to have a limited influence in this study area. Those environmental controls, where significant, appear logical and can be related back to the site conditions, but it remains surprising that these relationships cannot be applied more widely. The progressive failure model [*Bjerrum*, 1967] suggests that after the slope has entered the tertiary phase of deformation as represented by a linear trend in inverse velocity time space, the controls on failure timing are dictated entirely by the mechanical evolution of the rock mass, so environmental variability has little influence upon failure timing. This characteristic has been widely observed in the deformation of other failing slopes and in this inventory appears to be reflected in the degree of disruption to the slope surface and rockfall generation.

[23] The monthly resolution of the sampling, the full range of precursors to failure, particularly in the days or hours prior to failure are unlikely to have been captured, particularly when, as has been demonstrated, these rockfalls maybe superimposed on the cliff face. With such accelerating behavior, others have suggested that the development of failure may be subject to some degree of self-organization [*Zvelebil and Moser*, 2001]; the degree to which any given rockfall on the slope acts to redistribute stress, release strain, or add or remove load may here act to perpetuate the slope failure. In terms of the longer-term evolution of the cliffs this suggestion is unconventional, as here the implication is that small rockfalls, rather than acting to maintain a quasi-stable state or profile form, they may actually be a reflection of a slope moving toward a state of wider or larger-scale instability, supporting the suggestion that rockfalls may be out-of-equilibrium scale-free phenomena [*Dussauge et al.*, 2003]. Rockfalls may act as both stabilizing and destabilizing phenomena simultaneously, in which the largest rockfalls result from an imbalance in their relative effect. Precursory rockfalls also appear often to be concentrated around the extremities of the ultimate failure scar, particularly the lower edge, possibly reflecting the zone of maximum relative strain between stable and unstable zones of the rock mass. This observation may be specific to the slopes monitored here, where the dominant shale is closely jointed.

[24] A qualitative model of this time-dependence in rockfall generation is illustrated in Figure 8. During period 'a' the rock face undergoes a background level of material detachment as a product of weathering and physical detachment of surface material. Environmental events such as storms instigate an increased number of rockfalls, many of which are small in size. The result is a redistribution of stress within the rock mass, leading to damage accumulation via crack development (Figure 6, stage 'b'). Damage incurred is considered both cumulative and irreversible in this context, though may vary in other situations if for example open joints are recemented by infill. Periods of relative quiescence in rockfall activity can be mirrored by events of different intensity and duration (Figure 6, stage 'c'), each of which act to push the rock mass toward a critical strain related threshold, marked in Figure 6 by the dashed horizontal line. In some instances the rock mass may reside in a condition very close to instability in the absence of an event to instigate the transition to instability (Figure 6, stage 'd'), though during particularly acute environmental conditions this period may not occur. The rock mass may

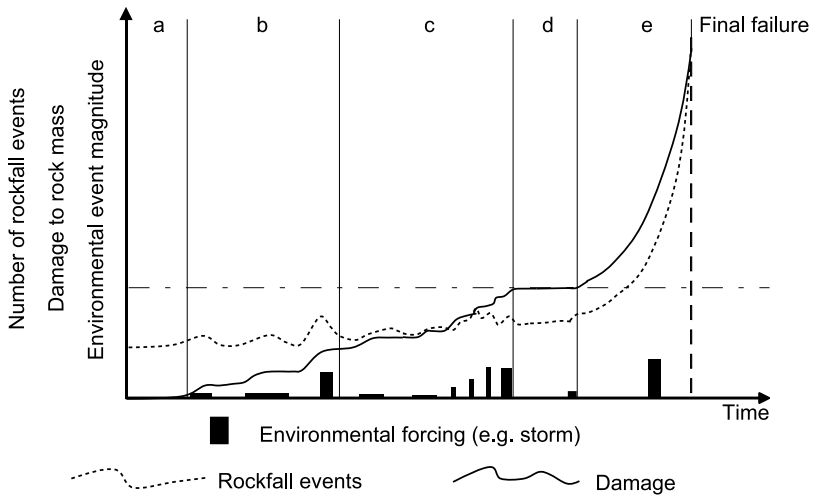

Figure 8. Schematic model of the development of a large slope failure, via a process of shedding of surficial material through rockfall and the accumulation of damage to the rock mass.

however exist in a state close to this threshold for a significant period without entering the final phase of failure, potentially explaining why many failures occur without an apparent trigger, often in apparently inert conditions. After the threshold is crossed, here defined as the point after which the dominant controls on rock mass failure shift from external to internal, the rock mass enters a tertiary phase of failure, characterized by a hyperbolic increase in the accumulation of strain (Figure 6, stage 'e'). The monitoring data presented above suggests that the occurrence of increasingly large rockfalls in the months prior to failure show this temporal pattern also. Environmental events during this period have little or no discernable influence on the rate of strain accumulation; the failure would appear to adhere to linear relationship within inverse velocity against time space. Theoretically with adequate sampling this may allow the failure time to be predicted in advance. All sections of the slope could be suggested to reside at some point on this curve as a function of the ratio of accumulated damage versus critical level required for failure at each location. Hence the position on the curve is a function of event history and the intensity of environmental forcing. The time between the point of transition from the secondary to tertiary phase of behavior here appears to be scale-dependent but it remains difficult to identify the shift in behavior particularly in the early tail of the hyperbolic curve given the variability of the baseline rate of rockfall activity. Notwithstanding this, the magnitude and timing of precursors is scale-dependent. It is tenuous to suggest that the apparent initial displacement observed, the primary period of activity, some months before several of the large failures is indeed a shift in rock mass behavior rather than a perturbation in the baseline rates of failure on the cliff face, but this is an interesting line of further enquiry. The relationship between small and large events in brittle systems has been previously addressed, particularly with reference to earthquake triggering [*Helmstetter*, 2003; *Malamud et al.*, 2004; *Main*, 2000]. Extrapolations can be made with regards the causation acting across the spectrum of event sizes. Interestingly, if the smaller rockfalls observed result in a feedback perpetuating larger slope failure from a slope management perspective small rockfalls are relatively easy to control.

6. Conclusions

[25] The results demonstrate that the coastal cliffs studied behave in a manner similar to nonmarine rock faces, with a limited control of wave action at the toe of the cliff face. This questions the role of notch development and failure propagation in the evolution of these coastal cliffs. Furthermore the environmental control on failure occurrence is limited, and appears to be scale-bound only influencing the smallest failures. The results presented suggest that precursors are scale-dependent, as observed by amongst others *Suwa* [1991], and that as a result rockfalls can potentially be viewed and quantified as precursory behavior prior to a larger slope failure. The rockfall inventory developed shows that rockfall volumes are scale-invariant, albeit over a limited range of magnitudes. The logical extrapolation of this behavior is the consideration of time-dependent sequences of events sourced from any particular rock face section, with accelerating activity prior to failure. The approach of previous inventories based upon the measurement of rockfall debris rather than scar have been unable to discern this sequencing. This data presented appears to bring together the scaling effects found in many other rockfall inventories, with models of self-organization, which have been suggested to lie beneath failure magnitude-frequency patterns, to time-dependent models of failure development and initiation. The intensive monitoring using 3D laser scanning has been shown to be capable of capturing the spatial precision to obtain a close to full magnitude-frequency distribution.

[26] The level of precursory activity has been related to the magnitude of the final failure geometry, and the time period within which precursory behavior is discernable from a background level of rockfall activity increases with final failure volume. The significant limitation of the approach is the temporal frequency of sampling that by definition is unable to capture the final acceleration of activity prior to failure. The degree to which this approach is effective on other rock faces is ultimately a function of

the level of material loss leading to failure that is a product of the material properties and environmental conditions. In such instances greater advances maybe made by directly monitoring the deformation (displacement) field across the rock face. Laser scanning technology is well suited to this and with phase-based laser scanners the precision required is easily obtainable. Ongoing work is focusing on improving further the temporal evolution of failure by developing permanently installed laser scanning systems giving a real-time assessment of rockfall activity and slope surface deformations.

[27] **Acknowledgments.** The support of Cleveland Potash Ltd., nGridWireless, Measurement Devices Limited and the contributions of an anonymous donor to the Geography Department, Durham University have supported this research; www.bigf.ac.uk is acknowledged for the GPS control used in survey set-up. The contribution of the UK Meterological Office, PD Ports Ltd, and the British Oceanographic Data Centre in providing additional environmental data is gratefully acknowledged.

References

Abellan, A., N. J. Rosser, J. M. Vilaplana, D. Garcia, J. Calvet, and S. A. Dunning (2007), Terrestrial laser scanning for rockslope monitoring and joint orientation: The influence of the point density, paper presented at General Assembly, Eur. Geosci. Union, Vienna.

Adler, B., Y. Hong, G. Huffman, A. Negri, and M. Pando (2006), Towards a quasi-global precipitation-induced landslide detection system using remote sensing information, *Eos Trans. AGU*, *87*(36), Joint Assem. Suppl., Abstract H23A-04.

Agar, R. (1960), Post-glacial erosion of the North Yorkshire coast from the Tees Estuary to Ravenscar, *Proc. Yorkshire Geol. Soc.*, *32*(4), 409–428.

Amitrano, D., J. R. Grasso, and G. Senfaute (2005), Seismic precursory patterns before a cliff collapse and critical point phenomena, *Geophys. Res. Lett.*, *32*, L08314, doi:10.1029/2004GL022270.

Bak, P., C. Tang, and K. Wiesenfeld (1987), Self-organized criticality: An explanation of 1/f noise, *Phys. Rev. Lett.*, *59*, 381–384.

Bjerrum, L. (1967), Progressive failure of slopes of over consolidated plastic clay and clay shales, *J. Soil Mech. Found. Div. Am. Soc. Civ. Eng.*, *93*, 1–49.

Crosta, G., and F. Agliardi (2003), Failure forecast for large rock slides by surface displacement measurements, *Can. Geotech. J.*, *40*, 176–191.

Day, R. W. (1997), Case studies of rockfall in soft versus hard rock, *Environ. Eng. Geosci.*, *3*(1), 133–140.

Densmore, A. L., M. A. Ellis, and R. S. Andersen (1998), Landsliding and the evolution of normal-fault-bounded mountains, *J. Geophys. Res.*, *103*(B7), 15,203–15,219.

Dorren, L. K. A. (2003), A review of rockfall mechanics and modeling approaches, *Prog. Phys. Geogr.*, *27*(1), 69–87.

Dussauge, C., J. Grasso, and A. Helmstetter (2003), Statistical analysis of rockfall volume distributions: Implications for rockfall dynamics, *J. Geophys. Res.*, *108*(B6), 2286, doi:10.1029/2001JB000650.

Dussauge-Peisser, C., A. Helmstetter, J.-R. Grasso, D. Huntz, P. Desvarreux, M. Jeannin, and A. Giraud (2002), Probabilistic approach to rockfall hazard assessment: Potential of historical data analysis, *Nat. Hazards Earth Syst. Sci.*, *2*, 15–26.

Evans, S. G., R. H. Guthrie, N. J. Roberts, and N. F. Bishop (2007), The disastrous 17 February 2006 rockslide-debris avalanche on Leyte Island, Philippines: A catastrophic landslide in tropical mountain terrain, *Nat. Hazard Earth Syst. Sci.*, *7*, 89–101.

Fehler, M., A. Jupe, and H. Asanuma (2001), More than clouds: New techniques for characterizing reservoir structure using induced seismicity, *Leading Edge*, *20*, 324–328.

Fuzukono, T. (1984), A new method for predicting the failure time of a slope, Proceedings of the IVth International Conference and Field Workshop on Landslides, Jpn. Landslide Soc., Tokyo.

Grasso, J. R., and D. Sornette (1998), Testing self-organized criticality by induced seismicity, *J. Geophys. Res.*, *103*(B12), 29,965–29,987.

Guzzetti, F., B. D. Malamud, D. L. Turcotte, and P. Reichenbach (2002), Power-law correlations of landslide areas in Central Italy, *Earth Planet. Sci. Lett.*, *195*, 169–183.

Guzzetti, F., P. Reichenbach, and G. F. Wieczorek (2003), Rockfall hazard and risk assessment in the Yosemite Valley, California, USA, *Nat. Hazards Earth Syst. Sci.*, *3*, 491–503.

Hall, K. (1988), A laboratory simulation of rock breakdown due to freeze-thaw in a maritime Antarctic environment, *Earth Surf. Processes Landforms*, *13*, 369–382.

Helmstetter, A. (2003), Is earthquake triggering driven by small earthquakes?, *Phys. Res. Lett.*, *91*, 058501.

Hergarten, S. (2003), Landslides, sandpiles and self-organized criticality, *Nat. Hazards Earth Syst. Sci.*, *3*, 505–514.

Hovius, N., C. P. Stark, and P. A. Allen (1997), Sediment flux from a mountain belt derived by landslide mapping, *Geology*, *25*, 231–234.

Howarth, M. K. (1992), The ammonite family Hildoceratidea in the Lower Jurassic of Great Britain, *Monogr. Palaeontogr. Soc.*, *586*, 1–106.

Huggel, C., S. Zgraggen-Oswald, W. Haeberli, A. Polkvoj, I. Galushkin, I., and S. G. Evans (2005), The 2002 rock/ice avalanche at Kolka/Karmadon, Russian Caucasus: Assessment of extraordinary avalanche formation and mobility, and application of Quickbird satellite imagery, *Nat. Hazards Earth Syst. Sci.*, *5*, 173–187.

Hungr, O., S. G. Evans, and J. Hazzard (1999), Magnitude and frequency of rock falls and rock slides along the main transportation corridors of southwestern British Columbia, *Can. Geotech. J.*, *36*, 224–238.

Kilburn, C. J. (2005), Fracturing as a quantitative indicator of lave flow dynamics, *J. Volcanol. Geotherm. Res.*, *132*, 209–224.

Lim, M., D. N. Petley, N. J. Rosser, R. J. Allison, A. J. Long, and D. Pybus (2005), Combined digital photogrammetry and time-of-flight terrestrial laser scanning for monitoring cliff evolution, *Photogramm. Record*, *20*, 109–129.

Main, I. (2000), A damage mechanics model for power-law creep and earthquake aftershock and foreshock sequences, *Geophys. J. Int.*, *147*(1), 151–161.

Malamud, B. D., D. L. Turcotte, F. Guzzetti, and P. Reichenbach (2004), Landslide inventories and their statistical significance, *Earth Surf. Processes Landforms*, *29*, 687–711.

Palus, M., D. Novotna, and J. Zvelebil (2004), Fractal rock slope dynamics anticipating a collapse, *Phys. Rev. E.*, *70*, 036212-1–036212-7.

Petley, D. N. (2004), The evolution of slope failures: Mechanisms of rupture propagation, *Nat. Hazards Earth Syst. Sci.*, *4*, 147–152.

Petley, D. N., T. Higuchi, S. A. Dunning, N. J. Rosser, D. J. Petley, M. H. K. Bulmer, and K. J. Carey (2005), A new model for the development of movement in progressive landslides, in *Landslide Risk Management* [CD-ROM], edited by O. Hungr et al., A. A. Balkema, Amsterdam.

Pralong, A., C. Birrer, W. A. Stahel, and M. Funk (2005), On the predictability of ice avalanches, *Nonlinear Processes Geophys.*, *12*, 849–861.

Rapp, A. (1960), Recent development of mountain slopes in Kärkevagge and surroundings, northern Scandinavia, *Geogr. Ann.*, *42*, 71–200.

Rosser, N. J., M. Lim, and D. N. Petley (2005), The use of terrestrial laser scanning for monitoring the process of hard rock coastal cliff erosion, *Q. J. Eng. Geol. Hydrogeol.*, *35*, 71–78.

Saito, M., and H. Uezawa (1961), Failure of soil due to creep, paper presented at Fifth International Conference on Soil Mechanics and Foundation Engineering, Int. Soc. of Soil Mech. and Geotech. Eng., Montreal, Que., Canada.

Sass, O. (2005a), Spatial patterns of rockfall intensity in the northern Alps, *Z. Geomorphol. Suppl. Band*, *138*, 51–65.

Sass, O. (2005b), Temporal variability of rockfall in the Bavarian Alps, Germany, *Arct. Antarct. Alp. Res.*, *37*(4), 564–573.

Simonett, D. S. (1967), Landslide distribution and earthquakes in the Bewani and Torricelli Mountains, New Guinea, in *Landform Studies From Australia and New Guinea*, edited by J. N. Jennings and J. A. Mabutt, pp. 64–84, Cambridge Univ. Press, Cambridge, U.K.

Suwa, H. (1991), Visual observed failure of a rock slope in Japan, *Landslide News*, *5*, 8–9.

Suwa, H., M. N. Hirano, and K. Okunishi (1991), Rock failure process of cutting slope in Shimanto geologic belt in Kyushu, Japan, *Ann. Disaster Prev. Res. Inst.*, *31*(B-1), 139–152.

Szwedzicki, T. (2003), Rock mass behavior prior to failure, *Int. J. Rock Mech. Min. Sci.*, *40*, 573–584.

Turcotte, D. L. (1997), *Fractals and Chaos in Geology and Geophysics*, 2nd ed., Cambridge Univ. Press, Cambridge, U.K.

Varnes, D. J. (1983), Time-deformation relations in creep to failure of Earth materials, paper presented at 7th Southeast Asian Geotechnical Conference, Southeast Asian Geotech. Soc., Pathumthani, Thailand.

Vidrih, R., M. Ribicic, and P. Suhadolc (2001), Seismogeological effects on rocks during the 12 April 1998 upper Soca Territory earthquake (NW Slovenia), *Tectonophysics*, *330*(3), 153–175.

Voight, B. (1988), A method for prediction of volcanic eruption, *Nature*, *332*, 125–130.

Walder, J. S., and B. Hallet (1986), The physical basis of frost weathering: Toward a more fundamental and unified perspective, *Arct. Alp. Res.*, *18*, 27–32.

Willenberg, H., T. Spillmann, E. Eberhardt, K. Evans, S. Loew, and H. R. Maurer (2002), Multidisciplinary monitoring of progressive failure pro-

cesses in brittle rock slopes—Concepts and system design, in *Proceedings of 1st European Conference on Landslides*, pp. 477–483, A. A. Balkema, Amsterdam.

Zvelebil, J., and M. Moser (2001), Monitoring based time-prediction of rockfalls: Three case histories, *Phys. Chem. Earth, Ser. B*, *26*(2), 159–167.

R. Allison, University of Sussex, Sussex House, Brighton, BN1 9RH, UK. (r.j.allison@sussex.ac.uk)

S. Dunning, D. Petley, and N. Rosser, International Landslide Centre, Institute of Hazard and Risk Research, Geography Department, Durham University, Durham. DH1 3LE, UK. (s.a.dunning@dur.ac.uk; d.n.petley@dur.ac.uk; n.j.rosser@dur.ac.uk)

M. Lim, School of Civil Engineering and Geosciences, University of Newcastle upon Tyne, NE1 7RU, UK. (michael.lim@ncl.ac.uk)